LiDAR-Derived Surface Roughness Texture Mapping: Application to Mount St. Helens Pumice Plain Deposit Analysis

Patrick L. Whelley, Lori S. Glaze, Eliza S. Calder, and David J. Harding

***Abstract*—Statistical measures of patterns (textures) in surface roughness are used to quantitatively differentiate volcanic deposit facies on the Pumice Plain, on the northern flank of Mount St. Helens (MSH). Surface roughness values are derived from a Light Detection and Ranging (LiDAR) point cloud collected in 2004 from a fixed-wing airborne platform. Patterns in surface roughness are characterized using co-occurrence texture statistics. Pristine-pyroclastic, reworked-pyroclastic, mudflow, boulder beds, eroded lava flows, braided streams, and other units within the Pumice Plain are all found to have significantly distinct roughness textures. The MSH deposits are reasonably accessible, and the textural variations have been verified in the field. Results of this work indicate that by affecting the distribution of large clasts and tens-of-meter scale landforms, modification of pyroclastic deposits by lahars alters the morphology of the surface in detectable quantifiable ways. When a lahar erodes a pyroclastic deposit, surface roughness increases, as does the randomness in the deposit surface. Conversely, when a lahar deposits material, the resulting landforms are less rough but more random than pristine pumice-rich pyroclastic deposits. By mapping these relationships and others, volcanic deposit facies can be differentiated. This new method of mapping, based on roughness texture, has the potential to aid mapping efforts in more remote regions, both on this planet and elsewhere in the solar system.**

***Index Terms*—Light Detection and Ranging (LiDAR), Mount St. Helens (MSH), surface roughness, texture, volcanology.**

I. Introduction

SPECTRAL remote sensing is well suited for differentiating domains based on chemistry and mineralogy. The addition of topographic analyses can augment spectral interpretations, e.g., [1]–[3] as compositionally identical materials can have distinct morphologies and thus represent different modes of origin. This is particularly relevant for volcano remote sensing where vastly different emplacement mechanisms can produce deposits with the same mineralogy. For example, effusive lava flows and explosive pyroclastic flow and fall deposits all of dacitic composition are present at Lascar Volcano, Chile [4] and Mount St. Helens (MSH), Washington [5]. Furthermore, reworked sediment derived from volcanic deposits is spectrally difficult to distinguish from its primary source (e.g., pyroclastic flow deposit and braided stream bed rich in pyroclastic material). In this case, these two landforms have strikingly different morphologies (digitate deposits with broad planar tops, e.g., [6] and flat-bottomed channels bound laterally by terraces, e.g., [7]) and are therefore easily differentiated in the field. However, where volcanoes are too remote for adequate field measurements to be made quickly, or where deposits are too vast for their context to be understood, morphologic analysis of remote sensing data is necessary, e.g., [8]–[11]. A new method that can quantitatively and efficiently identify and compare patterns in morphologic measurements would improve the utility of such measurements by providing a framework for comparing deposit morphology.

The technique presented here uses patterns in surface roughness (roughness textures) to statistically differentiate morphologic units. The MSH *Pumice Plain* is chosen as a study area (Fig. 1), because it provides a dynamic landscape with a variety of morphologies, the geologic history has been well characterized, and high-fidelity topography data (discussed in Section II-B) are freely available.

Manuscript received October 10, 2011; revised November 2, 2012; accepted December 21, 2012. Date of publication March 8, 2013; date of current version November 26, 2013. LiDAR data of the MSH Pumice Plain were acquired by Terrapoint, under contract to NASA, in collaboration with the Puget Sound LiDAR Consortium, with funding from the NASA Solid Earth and Natural Hazards Program. A NASA Graduate Student Research Program Fellowship Grant:NNX08AT55H generously supported P. L. Whelley.

P. L. Whelley was with the Department of Geology, University at Buffalo SUNY, Buffalo, NY 14260-3050 USA and is now with Earth Observatory of Singapore, Nanyang Technological University, Singapore 639798 (e-mail: pwhelley@ntu.edu.sg).

L. S. Glaze and D. J. Harding are with Planetary Geodynamics Laboratory, NASA Goddard Space Flight Center, Greenbelt, MD 20771 USA (e-mail: lori.s.glaze@nasa.gov; David.J.Harding@nasa.gov).

E. S. Calder is with the Department of Geology, University at Buffalo SUNY, Buffalo, NY 14260-3050 USA (e-mail: ecalder@buffalo.edu).

Digital Object Identifier 10.1109/TGRS.2013.2241443

II. Background

A. MSH 1980 Pumice Flow Deposits

The climactic 1980 eruptions of MSH began on the morning of May 18th, with a massive debris avalanche followed by a lateral explosion of the newly exposed lava dome [12], [13]. The subsequent plinian and vulcanian-style eruptions (on May 18 and 25, June 12, July 22, and August 7, October 16–18) produced pyroclastic flow deposits in the valley between the MSH north flank and Johnston ridge, forming the Pumice Plain (Fig. 1) [6], [14], and [15].

The pyroclastic flow deposits are rich in pumice, ash, and shards of lithic material from ash to block size ($>$ 64 mm) [16]. When fresh, the deposits ranged from having sheet-like planar morphology to a fan of overlapping elongate tongues 15 to 75 m wide with lobate snouts and raised levees [17]. At their margins, individual deposit units were 1 to 4 m thick and 10 m or thicker in the interior [6].

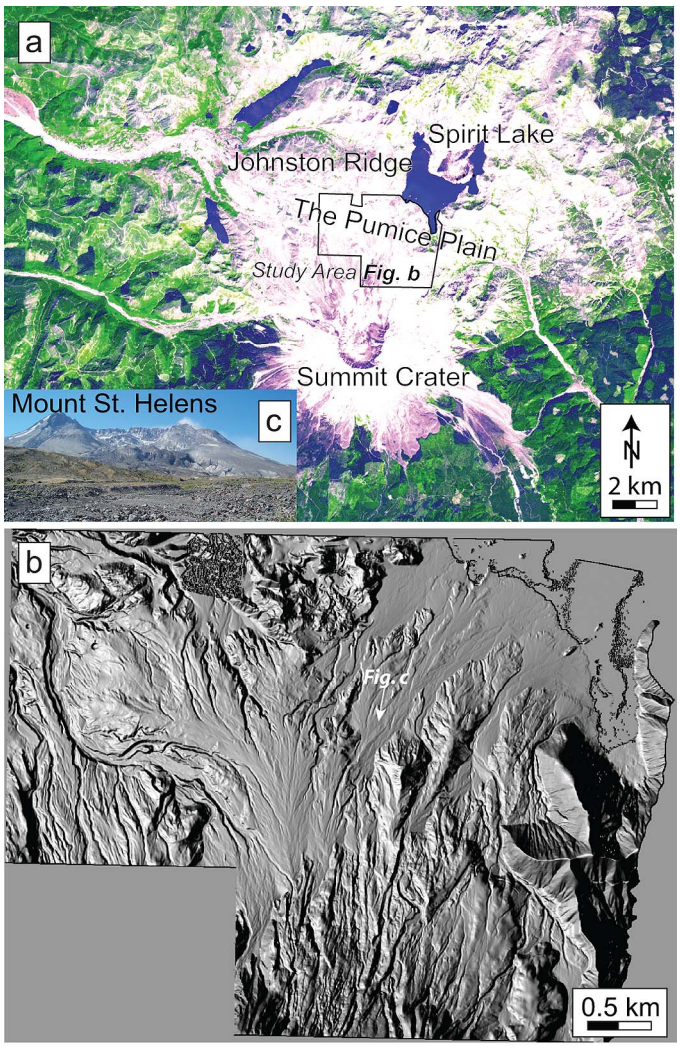

Fig. 1. (a) ASTER image #20000808192755 showing the study area (b) and Mount St. Helens' summit crater. (b) Shaded relief map derived from airborne LiDAR ground points collected on November 20, 2004 by Terrapoint LLC. (c) View of Mount St. Helens over the Pumice Plain, from southern bank of Spirit Lake taken on August 13, 2010.

The climactic eruption of 18 May also produced lahars by melting snow and ice both on the volcanic edifice and trapped within the debris avalanche. The erosive power of the flows, both from the climactic eruption as well as those that occurred subsequently, quickly carved channels through the fresh Pumice Plain [18], eventually affecting nearly the entire watershed draining the mountain [19] and 80% of the Pumice Plain [20], [21]. Lahar production in this area continued for a decade [22] with major erosional events occurring in 1982, 1983, and 1984 [23]. When lava dome growth resumed in 2004, lahars were again produced [24], further modifying the deposits of the Pumice Plain. The surface of the Pumice Plain as it was in 2004, therefore, represents that of the original morphology with 24 years of post-eruption modification. This analysis shows that by quantifying deposit morphology using high-resolution topography and statistical tools, the Pumice Plain primary deposits remain identifiable. The approach developed here allows primary morphology and emplacement surfaces to be easily distinguished from later, secondary processes within compositionally similar terrain.

TABLE I
LIST OF ALL VARIABLES USED AND, WHERE APPLICABLE, THE RANGE OF INPUT VALUES

Variable	Description	Values	Unit
R_n	Roughness neighborhood (size of roughness pixel)	5	Meters
W	Search and base window size (X and Y)	7, 11, 15, 31, 51	R_n pixels
δ	Linear offset of search window from base	1	Pixels
θ	Angular offset of search window from base	45	Degrees
Pr(x)	Probability function		
C_{ij}	Co-occurrence probability		
P_{ij}	Measured co-occurrences		
Q	Number of quantized roughness values	64	Integer
r	Roughness values on raster		Meters
μ_x	Mean of C_{ij} matrix row sums		
μ_y	Mean of C_{ij} matrix column sums		
σ_x	Standard deviation of C_{ij} matrix row sums		
σ_y	Standard deviation of C_{ij} matrix column sums		

B. Airborne Light Detection and Ranging

Light detection and ranging (LiDAR) altimetry is a method of accurately evaluating the location of a surface by reflecting pulses of light off an interface, detecting their return, and precisely measuring the two-way travel time. LiDAR is commonly used in atmospheric studies, e.g., [25] and geomorphology, e.g., [26]. LiDAR data are now increasingly being used for mapping volcanoes and their products by characterizing the intensity of laser returns from lava flows [27] or deriving highly accurate digital elevation models (DEMs) of active lava flows [28] and other deposits, e.g., [24], [29]. The high densities of LiDAR observations have also been used to map surface roughness and differentiate lava flow terrains [30]. Here, we use surface roughness to study pyroclastic materials and differentiate between primary and secondary flow-derived surfaces.

C. Surface Roughness

Surface roughness is a measure of elevation variability normalized by slope. By interrogating multiple neighboring LiDAR returns as a group, surface roughness can be quantified in a number of ways, including: taking the difference between the maximum and minimum elevation [31], the standard deviation of elevations [32], root mean square of elevation differences [30], the standard deviation of de-trended elevations to first [33], [34] or second order [35], [36], and the difference of slopes at multiple scales [37]. In all cases, a roughness neighborhood (R_n) (Table I: variables list) is chosen, which defines an area that outlines the data points involved in the roughness calculation. Elevation points that fall within the R_n are included in the roughness calculation, and a larger R_n includes more elevation points in each calculation. For a feature on the ground to affect the calculated surface roughness, it must produce a difference in elevation within the R_n. Further, the variations in elevation must be larger (in the vertical dimension) than the relative accuracy of the elevation measurement. Regardless of what statistic is used to characterize roughness, its value depends on the size of the neighborhood and the physical

properties of the surface material. Here, roughness is calculated after removing regional slope, following [33] (Section III-B). Patterns are then quantified in surface roughness using textural statistics after [38] to distinguish surface materials.

D. Texture

Textures are patterns in spatial data. The statistical equations to quantify textures in spatial data were first defined to identify patterns in gray-scale air photos [38]. Later, the same texture statistics were used to differentiate agricultural environments [39] and varieties of sea-ice [40] in radar-reflectance data. The texture of any surface characteristic (e.g., spectral reflectance, surface classification [41], slope, or surface roughness) can be found using the same equations by substituting the surface characteristic value for the gray value in equations from [38]. In this paper, we explore the texture of surface roughness because it reflects the different initial depositional and/or erosional history of the deposits and thus has a physical significance that can assist in deposit interpretation. Surface roughness textures are straightforward to calculate from commonly available elevation data and contain interpretable information about the depositional style and erosive history of the surface.

III. Methodology

A. MSH LiDAR Data

LiDAR data of the MSH Pumice Plain were acquired on November 20, 2004 from a fixed-wing airborne platform by Terrapoint, under contract to NASA, in collaboration with the Puget Sound LiDAR Consortium, with funding from the NASA Solid Earth and Natural Hazards Program. Individual points have a 0.75 m footprint, with a spacing of 1.8 m and an absolute precision of 0.5 m (horizontal) and 0.15 m (vertical) [42]. Each pulse of 1064 nm wavelength light sent by the LiDAR instrument produced multiple laser reflections. The reflection that takes the longest amount of time to return from the target to the detector is classified as the ground return. To prevent vegetation, which is now re-growing on the Pumice Plain, e.g., [43], from being included in the analysis and producing anomalous roughness, only ground returns are used in the analysis.

B. Calculating Roughness

Local surface roughness is calculated directly from the LiDAR data by first removing regional trends from the ground elevation measurements. De-trending is achieved following [33] by fitting a regression surface to all measured ground points within a roughness neighborhood (R_n). The standard deviation of the residuals (elevation measurements minus the fitted values) is the definition chosen here to characterize roughness. This roughness value is then assigned to a corresponding pixel; all of the pixels arranged together produce a roughness map [Fig. 2(a)]. To ensure that meaningful roughness calculations are made, we require 95% of pixels to include a minimum of four elevation points. The smallest R_n where this is achieved is 5 m (Table II). This is important because, by definition, three points are necessary to define a plane, so more than three are necessary for the resulting residuals to be meaningful. An R_n of 5 m was therefore used across the Pumice Plain. After

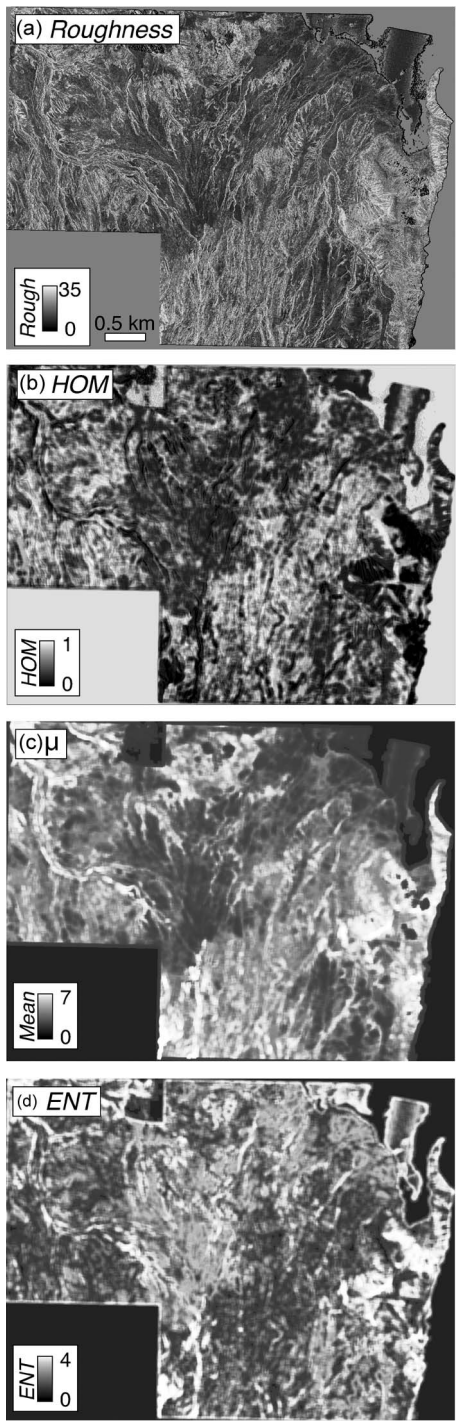

Fig. 2. (a) Surface roughness map of MSH Pumice Plain. (b)–(d) Example roughness textures: (b) *HOM* (c) μ (d) *ENT*. All are draped over shaded relief [Fig. 1(b)], $R_{\rm n} = 5, W = 11$.

TABLE II
MSH Roughness Neighborhood $(R_{\rm n})$ Dimensions *4*

$R_{\rm n}$ (m)	Mean Points/pixel	Minimum Points/pixel
2	2.5	0
3	6.8	1
4	11.4	2
5	17	4

Mean and minimum number of elevation points within 95% of pixels for different $R_{\rm n}$ values. $R_{\rm n} = 5$ was used in the analysis.

TABLE III
TEXTURE STATISTICS USED TO DEFINE PATTERNS IN SURFACE ROUGHNESS

Statistic	Equation	Explanation	Source	Number
Mean[1]	$\mu = \frac{\sum r}{Q}$	The average or roughness values within the base window		(3)
Variance[1]	$\sigma^2 = \frac{\sum r - \mu}{Q - 1}$	The variance of roughness values within the base window		(4)
Homogeneity	$HOM = \sum \frac{C_{ij}}{1 + \lvert i - j \rvert}$	Increases with local similarity in i and j	After [42]	(5)
Contrast	$CON = \sum C_{ij}(i - j)^2$	Increases with local variations in i and j	[41]	(6)
Dissimilarity	$DIS = \sum C_{ij}\lvert i - j \rvert$	Increases with local variations in i and j	[41]	(7)
Entropy	$ENT = \sum C_{ij} \log C_{ij}$	Increases with C_{ij} randomness	[41]	(8)
Second Moment	$SMT = \frac{\sum C_{ij}^2}{\sum C_{ij}}$	Increases with homogeneity within C_{ij}	After [40]	(9)
Correlation[2]	$COR = \sum \frac{(i - \mu_x)(j - \mu_y)C_{ij}}{\sigma_x \sigma_y}$	Increases with linear dependency of i and j	After [39]	(10)

[1] Where r is a roughness value within the base window and Q is the number of values.
[2] Where μ_x, and μ_y, are the means and σ_x, and σ_y are the standard deviations of the row (x) and column (y) sums of C_{ij}.

roughness maps are made, roughness textures are quantified using the methods described below.

C. Roughness Texture

To calculate roughness texture, roughness values are binned in 64 levels. This number of bins allows for fast computation while preserving the maximum amount of information [40] and follows [38] quantization of gray levels in photographs. Binning is achieved by fitting a step function [38] to the roughness data. Two search windows are then produced to interrogate the resulting 64-level roughness maps. Here, these two windows are referred to as *base* and *shift*. Both windows are W pixels square (Table I). The shift window is offset from the base window by δ pixels and θ degrees. The probability that binned (i.e., quantized) roughness value i occurs in the base window in the same place roughness value j occurs in the search window is the co-occurrence probability (C_{ij}) defined by the probability function $\Pr(x)$ after [38], [40] as

$$\Pr(x) = \{C_{ij}|(\delta, \theta)\}. \tag{1}$$

C_{ij} is found by

$$C_{ij} = \frac{P_{ij}}{\sum_{i,j=1}^{Q} P_{ij}} \tag{2}$$

where P_{ij} is the number of measured roughness co-occurrences (i and j) between the base and shift windows with a specified number of quantized roughness values, Q ($Q = 64$ in this case). The eight statistics in Table III are then applied to the co-occurrence matrix to produce texture maps [Fig. 2(b)–(d)]. Five values of W (Table I) are used that range from 7 to 51 pixels. Each texture statistic identifies a particular pattern and can be placed in one of the categories below.

—**Standard statistics**: These measures closely resemble familiar statistics and identify: Mean $(\boldsymbol{\mu})$: The average quantized roughness value within the base window, W pixels square. Rough regions have high μ [Fig. 2(c)]. Variance $(\boldsymbol{\sigma^2})$: A measure of the spread of values within the base window. Regions with variable roughness have high α^2.

—**Smoothness statistics**: These three measures identify local changes and characterize whether those changes are smooth or abrupt [41], [40]. Specifically, they measure:Homogeneity (***HOM***): How smoothly roughness values change within C_{ij}. *HOM* increases linearly with the reciprocal of the difference of each i and j pair. Regions with regular changes in roughness within W have high *HOM* [Fig. 2(b)]. Contrast (***CON***): How abruptly roughness values change within C_{ij}. CON increases with the square of the difference of each i and j pair. Regions with large, irregular changes in roughness within W have high *CON*. Dissimilarity (***DIS***): How different i and j are within C_{ij}. *DIS* increases linearly with the difference of each i and j pair. Regions with large changes in roughness within W have high *DIS*.

—**Uniformity statistics**: Both of these measures identify regions that have consistent or irregular values [39]. They determine: Entropy (***ENT***): How random the values in C_{ij} are. Increases in *ENT* are proportional to the log of C_{ij}. Regions with random distributions of roughness values within W have high *ENT* [Fig. 2(d)]. Second Moment (***SMT***): How similar i and j are within C_{ij}. *SMT* increases with the square of C_{ij}. Regions with uniform roughness values within W have high *SMT*. *SMT* is qualitatively an inverse of *DIS*.

—**Correlation statistic**: This unique measure identifies: Correlation (***COR***): How dependent i and j are on one another. *COR* increases when both i and j vary, with respect to the mean within C_{ij}. Regions with linear trends in roughness have high *COR* [38].

A map of each statistic is made separately where statistical values are assigned a gray level, and all eight are then collected in a stack analogous to spectral bands in a multispectral scene. Map stacks can then be compared to field observations (i.e., a

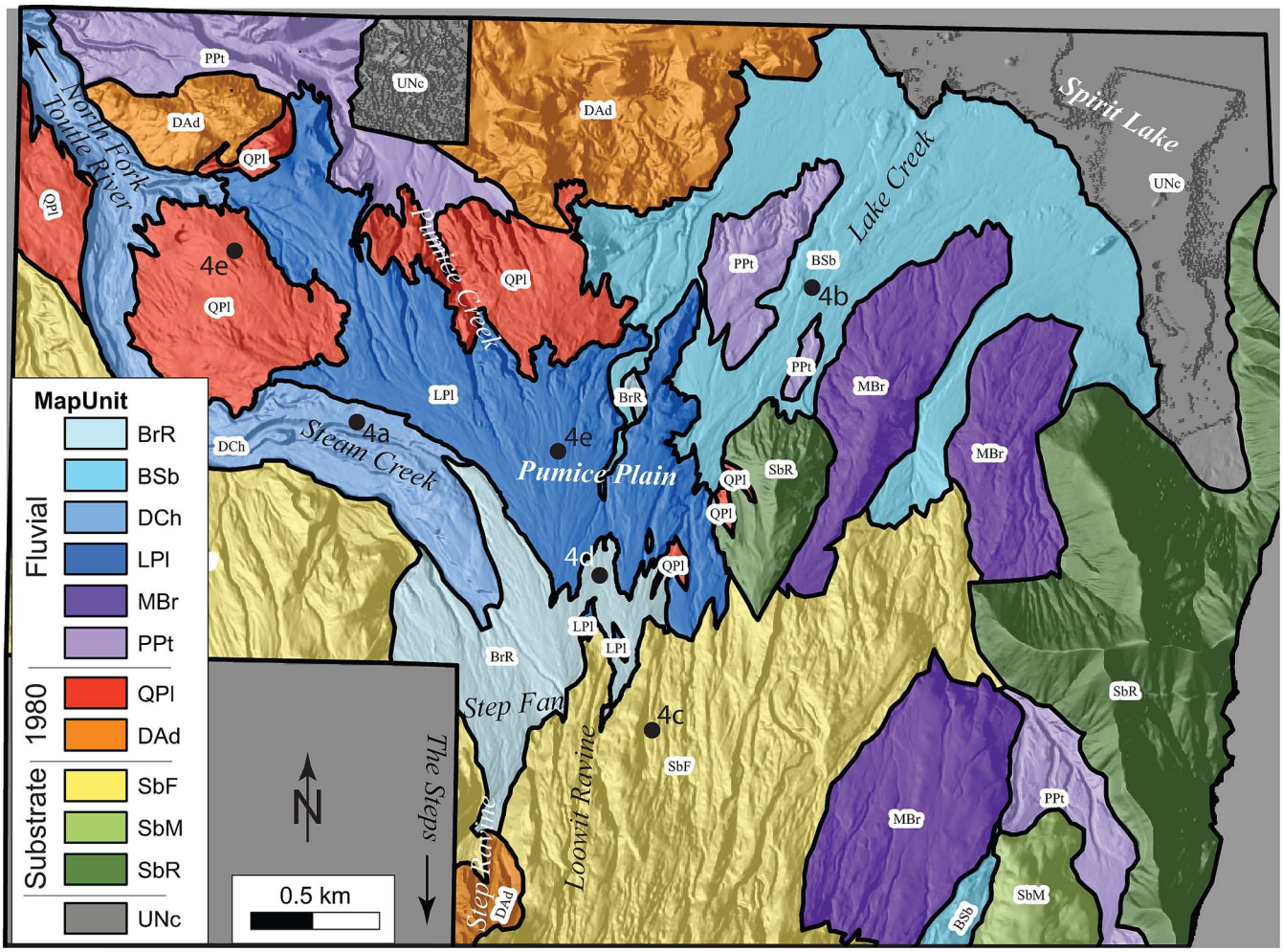

Fig. 3. Geomorphic units mapped using both field observations and the LiDAR-derived shaded relief map [Fig. 1(b)]. Black circles are the locations of photographs in Fig. 4. Place names are after [23].

geomorphic map, discussed in Section III-D) to interpret the geological significance of roughness texture.

D. Geomorphic Mapping

Geomorphic units were mapped based on data collected during a 2010 summer field season and using the shaded-relief map [Fig. 1(b)] derived from the LiDAR data described above (Section III-A). In the field, a pair of Leica SR20 Global Positioning System (GPS) receivers were used in kinematic mode to trace contacts and transects; and in static mode to record the locations of measurements and photographs. Post-processing of differential GPS data results in an absolute observation accuracy of ≤ 1 m.

To differentiate geomorphic units on the ground, shapes, and spacing of meter- to tens- of meters-scale features (e.g., ridges, fans, lobes, scarps, plateaus mounds, and hummocks) were recorded. Also, the principal lithofacies of each unit was noted (lava flows, lithics, ash, or pumice). The resulting map (Fig. 3) is described below. Later, statistical measures of separability are used to differentiate units using roughness texture (Section IV-C).

IV. Results

A. Pumice Plain Geomorphic Units

Based on the surface morphology, 11 separate units were identified on the Pumice Plain (Figs. 3 and 4; Table IV). They include pre-1980 substrate, pseudo-pristine depositional surfaces of the 1980 deposits, as well as post-depositional erosional surfaces. An additional 12th unit is unclassified (UNc), and it includes data holes and locations that are otherwise unreliable. In the unit descriptions below, conventional sedimentological terminology (silt, sand, gravel) is used for reworked deposits, and volcanology terms (ash, lapilli, blocks) are reserved for primary volcanic products.

Fluvial Units (modified volcaniclastics):

—BrR **Breccia Ridges:** [Fig. 4(d)]. Unconsolidated elongate bars containing 0.25 to 2 m blocks of lava at the base of the northern flanks of Mount St Helens. These bars are 2 to 3 m wide and stand 0.5 to 2 m above flat-bottomed troughs that are 5 to 8 m wide. The troughs contain considerably smaller (0.1–1 m) clasts and a coarse-ash matrix that is absent from adjacent bars. The uphill contact is defined by the break in slope at the base of the region know as the Stair-Steps [23].

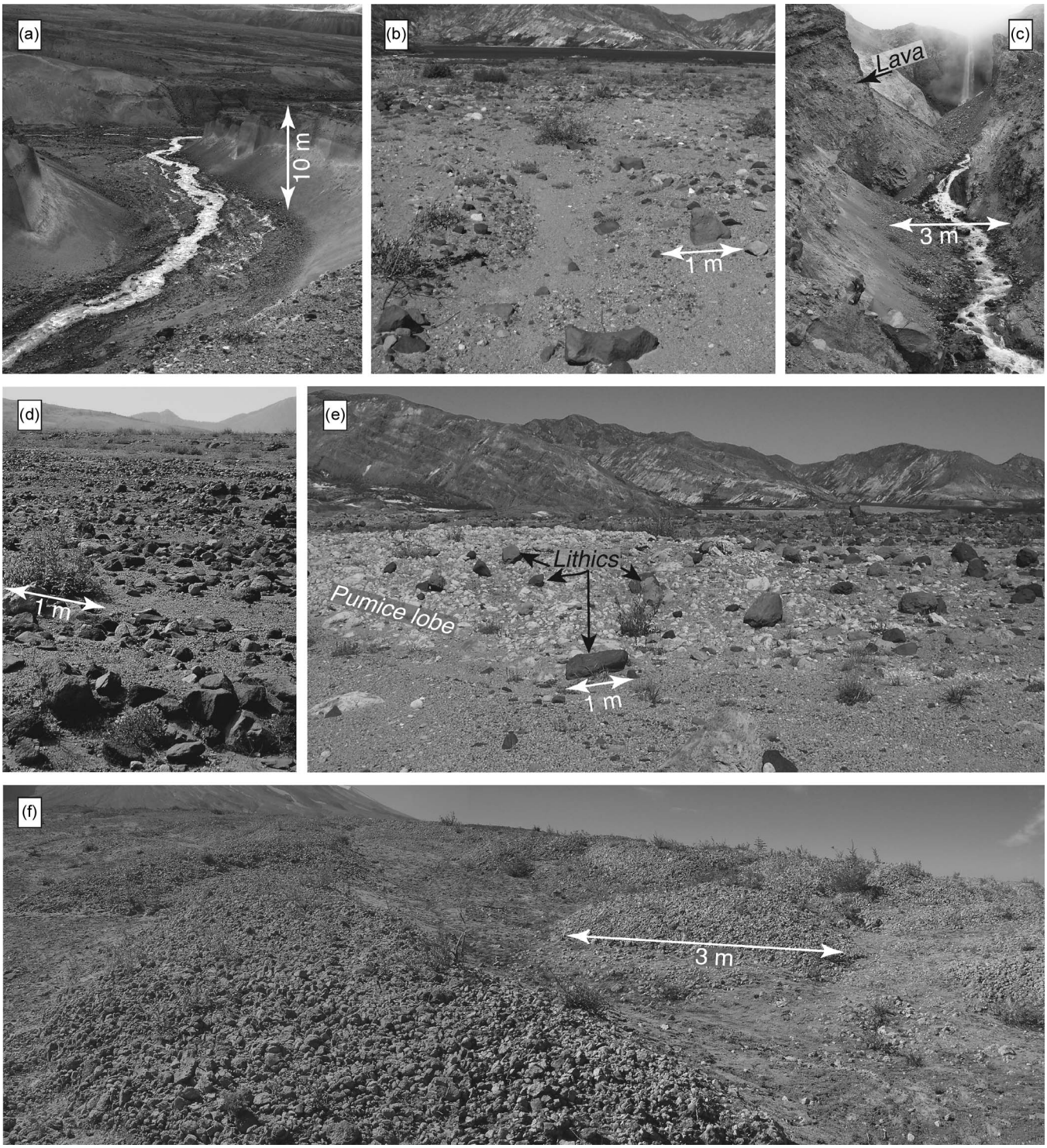

Fig. 4. Photographs of the typical aspect of six of the geomorphic units. Image locations provided in Fig. 3. (a) DCh: deep, steep walled active channel, (b) BSb: braided streambed stranded gravel bar, (c) SbF: cliffs of layered lava high on the southern slope, (d) BrR: lithics deposited by lahars (flow travelled from left to right), (e) LPl: a pumice lobe beneath a coarse lithic veneer, (f) QPl: Positive-relief pumice lobes with coarse clast-supported margins.

BrR represents the most proximal part of the Pumice Plain and correlates well with the Step Fan identified by [23]. The down-slope contact is defined by the appearance of pumice in the unit LPl. BrR likely corresponds to lahar deposits that have completely buried primary pumice deposits.

—BSb **Braided Streambed outwash fan:** [Fig. 4(a)]. Broad shallow channels with stranded gravel bars (10–20 m long) that make up a larger outwash plain. In the LiDAR-shaded relief, muted elongate hundred-meter-long lobes are evident. *In situ* observations indicate these lobes are made up of volcaniclastic sediment that ranges from sand to boulder sized. Sand-rich facies host decimeter to centimeter bedforms. Boulder bars, containing 1 to 3 m lava blocks, are common on the outer margins. BSb is distinguished from its

TABLE IV
SUMMARY OF GEOMORPHIC UNITS

Label	Unit	Description	Figure	Interpretation	Process
BrR	Breccia ridges	Rounded, elongate, bars of lithic blocks	4d	Thick lahar deposit [24]: Unit 1	Depositional
BSb	Braided streams	Gravel-rich islands bound by flat-bottomed, shallow active channels	4a	Active braided streams	Depositional
DCh	Deep steep-walled channels	Wide, active, stream channels with unconsolidated pumice and ash-rich walls and boulder-rich floor.	4b	Erosional pathways produced by lahars and post-1980 fluvial activity	Erosional
LPl	Lithic armored pumice lobes	Pumice lobes with a carapace of lithic blocks	4e	Thin lahar deposit over pumice lobes [24]: Unit 2	Depositional
MBr	Pumice and lithic mixed breccias	Fan-shaped deposits containing lithics and pumice		Reworked volcaniclastics	Depositional
PPt	Pumice-rich Plateaus	Planar, secondary pumice deposits		Stranded stream terraces, reworked	Depositional
QPl	Quasi-pristine Pumice lobes	Fans of 5 – 10 m rounded lobes with prominent coarse snouts of ~10 cm pumice	4f	Primary pumice rich ignimbrite deposited in 1980	Depositional
DAd	Debris Avalanche deposits	50 – 100 m stratified angular mounds of lava and tephra		Debris avalanche deposits from the 1980 eruptions	Depositional
SbF	Substrate Flank	Thin parallel ridges of dense lava exposed on a steep slope	4c	Lahar pathways	Erosional
SbM	Substrate Mounds	Patches of pyroclastic deposits that lack erosional channels		Reworked volcaniclastics that have efficient drainage	Depositional
SbR	Substrate Ridges	Triangular steep-sided ridges composed of lava and tephra		Pre-1980, dense lava and pyroclastic basement	Erosional
UNc	Unclassified	Unreliable or missing data			

bordering units by occupying the lower elevations. The BSb unit is interpreted to be made up largely of secondary volcaniclastics, transported, and deposited by fluvial processes.

—DCh **Drainage channels:** [Fig. 4(b)]. Wide (50–100 m) channels with 10 to 20 m high, nearly vertical walls. These features are unique to the Western Pumice Plain and comprise the widest and deepest erosion features, observable in the LiDAR shaded relief. The channels include Steam Creek (after [23]) and are incised into unconsolidated, primary, pumice- and ash-rich pyroclastic deposits; walls are unstable and subject to local occasional failure. Channel bottoms are characterized by dense, angular, decimeter (and up to 2 m) blocks of lava and ash-rich facies similar to that within the BSb unit and, near recent wall failures, sub-angular decimeter pumice. Contacts are defined by channel margins and headwalls of the failure scarps. The DCh unit is interpreted to have been formed by lahars immediately after the eruption and incised into primary pumice flow deposits (consistent with [23]). The channels, particularly Steam Creek, remain active and are the principal drainage for the northern flanks of MSH, eventually feeding into the North Fork of the Toutle River.

—LPl **Lithic-armored Pumice lobes:** [Fig. 4(e)]. This morphologic unit comprises fans of rounded lobes dissected by small gullies. These lobes have a core of decimeter-sized pumice and are clast-supported with a fine ash matrix. However, the lobes are armored with a carapace of discontinuous lithics (0.1–0.5 m in diameter), no more than one clast thick. Some lobes are only armored on their up-slope sides. A few lobes have noticeably coarser pumice at their margins than interiors; however, most are too obscured by the lithic veneer for internal structure to be observed. Narrow (∼10 m) gullies and their tributaries with curvilinear traces dissect the fans surface. LPl is interpreted as primary, distal facies pumice flow deposits that have been partially veneered by fluvial deposits from lahars, probably dating back to the early 1980s (see lahar map in [23]).

—MBr **Mixed Breccia units.** These units occupy gentle slopes, are unique to the eastern Pumice Plain, and are partially dissected by small (∼10 m) disconnected gullies. The surface lithofacies includes angular blocks of lava (typically 0.1–0.5 m but up to 1 m) and sub-rounded (< 0.5 m) pumice within an ash matrix. MBr is interpreted to be largely a secondary volcaniclastic deposit, potentially from multiple events, that have subsequently been partially incised by fluvial erosion.

—PPt **Pumice-rich plateaus.** This unit comprises flat-topped pumice-rich terraces, 1 to 3 m high and moderately dissected. The unit commonly contacts BSb, and is characterized by a distinctive dendritic network of shallow gullies (∼10 m). The plateaus are rich in sub-rounded, decimeter-sized pumice and ash, but lack the positive-relief structures found in QPl (below). The PPt unit is interpreted to be composed of secondary volcaniclastic deposits (from 1980s pumice-rich lahars) that have been moderately dissected, producing the dendritic networks of drainages.

1980 Eruptive units:

—QPl **Quasi-pristine Pumice lobes:** [Fig. 4(f)]. Rounded, stacked lobes on the western Pumice Plain. These lobes are typically 5 to 10 m wide and together produce larger fans with a branching morphology in the LiDAR shaded relief. Some lobes have levees raised 0.25 to 1 m above a flat central trough that makes up 80–90% of the lobe width. These lobes comprise decimeter pumice clasts and ash. QPl is distinguished from LPl by the absence of the coarse lithic veneer and from DCh, BSb, and PPt by the absence of incised drainage networks. QPl represents primary pumice lobes that have not been appreciably modified by post-emplacement erosion.

—DAd **Debris Avalanche deposits.** Hummocks of stratified lava blocks and tephra, mostly found at the northern extent of the Pumice Plain. These hummocks are 50 to 300 m across and contain strata similar to that found in SubR (below), 1–5 m thick lava and pyroclastics, but here with irregular dips. In the north, this unit is embayed by BSb, QPl, and PPt, and is slowly being dissected by fluvial processes responsible for DCh. DAd units are comprised of debris avalanche hummocks produced in the sector collapse phase of the 18 May 1980 eruption [14].

Substrate Units:

—SbF **Substrate Flanks:** [Fig. 4(c)]. Parallel linear ridges on a steep north-facing flank. The ridges are spaced 10 to 30 m (peak to peak) and comprise a coarse (2 to 5 m lava blocks) clast-supported lithic breccia without matrix. Troughs between the ridges include the Loowit and Step Ravines (after [23]) and are cut into polished mafic lava flows. The lower contact of this unit is defined by the break in slope, from steep flanks to flat-lying plain. SbF is made up of material from high-energy lahars, sufficient to transport 5 m blocks, and has been stripped of any pumice that was once deposited on its surface.

—SbM **Substrate Mounds.** Rounded knobs of unconsolidated material perched high on the north-facing flank. This is a pumice-rich unit, similar to PPt (and is made up of sand- to cobble-sized clasts), but has a rounded surface, and at the resolution of the DEM, lacks any drainage features. It is eroded at the margins by fluvial processes, likely those also responsible for BSb and PPt. Furthermore, the boundaries of SbM are defined by the location of active erosion at its margin. SbM contains reworked volcaniclastic material that is slowly being eroded by ongoing fluvial activity.

—SbR **Substrate Ridges.** Steep-sided, angular ridges in the eastern and central Pumice Plain. These ridges are local topographic highs, are embayed by all adjacent 1980 units, and therefore predate the eruptions. The ridges are made up of northward-dipping alternating layers (1 to 5 m thick each) of lava and pyroclastics. In a map of the pre-1980 MSH geology, [44] shows the eastern SbR unit as tertiary volcaniclastics (including tuffs and sedimentary rocks) and as a member of the Omanapecosh Formation. Consistent with [44], we interpret SbR to be pre-1980 substrate.

—UNc **Unclassified.** Contains insufficient data for classification.

B. Roughness Texture

Texture maps [Fig. 2(b)–(d)] derived from local surface roughness and based on *HOM*, *ENT*, and μ can be used to identify patterns caused by boulders, blocks, mounds, ridges, scarps, and channels. This information is combined in Fig. 5. The southeastern and western two-thirds of the map area (Fig. 5) are dominated by *HOM* (red layer) and μ (green layer), indicating that surface roughness is high and consistent (only small changes within W) throughout these orange regions. The central third has low μ and *HOM* but high *ENT* (blue layer) indicating that, while generally smooth, there are changes in surface roughness over small distances (within W). Red patches, present near the center of the map and in the southeast, are consistently smooth regions, whereas cyan regions are generally rough (high μ) but include random smooth patches that increase *ENT* and decrease *HOM*.

C. Separability of Geomorphic Units by Roughness Texture

Two different separability tests are performed to: (1) assess the influence of scale on calculated local roughness texture by varying W; and (2) determine if the geomorphic units have unique roughness textures that are statistically distinguishable.

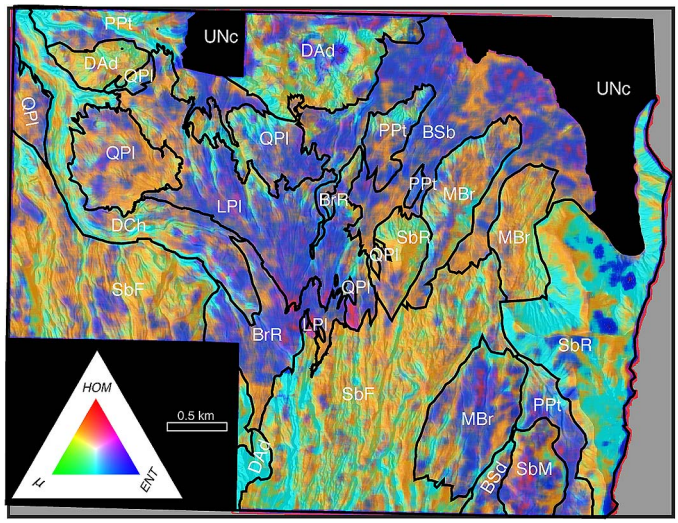

Fig. 5. Roughness textures with HOM displayed in red, ENT in blue and μ in green. Geomorphic unit boundaries are those shown in Fig. 3. In this figure, blue regions have high *ENT* indicating random roughness values. Orange regions are consistently rough (high *HOM* and μ). Cyan areas are also generally rough but have random smooth patches that increase *ENT*. Red areas (rare but present near a few blue patches) are consistently smooth regions (high *HOM* and low μ).

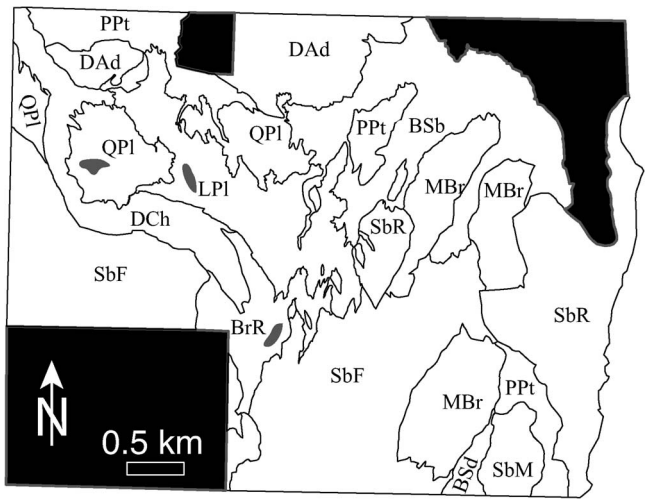

Fig. 6. Simplified geomorphic map that shows the regions (gray patches) used for the JM distance analysis (Table V).

For the first test, to determine the effect of scale on surface roughness, all-eight texture statistics are collected in a virtual stack so they can be processed in parallel. The Jeffries–Matusita (JM) distance [45], [46] is used to assess the affect of scale on calculated roughness texture. For each W, the JM distance compares the mean and covariance of map values from all layers in different regions. Here, each texture-statistic layer defines the map values, and three subsets within QPl, LPl, and BrR define the regions (Fig. 6). These geomorphic units are chosen to test the effect of scale because they have similar morphology (Fig. 4), are adjacent to each other, and are geologically similar (collections of lava blocks or pumice lobes). They therefore present a good test for unit separability.

In the JM distance test, covariance is calculated for regions two at a time, determining if the pair of geomorphic units are

TABLE V
JEFFRIES–MATUSITA DISTANCE FOR FIVE VALUES OF W

W[1]	Geomorphic Unit Pairs[2]		
	QPl & LPl	LPl & BrR	QPl & BrR
7	1.9992	2.0000	2.0000
11	2.0000	2.0000	2.0000
15	1.9985	2.0000	2.0000
31	1.9355	2.0000	2.0000
51	1.9212	1.9354	1.9981

[1] W is in R_n pixels
[2] A JM score ≥1.9 indicates the pairs are separable

separable. If JM ≥ 1.9, the unit pairs have distinguishable distributions of texture statistics. If $JM < 1.9$, the pair are statistically indistinguishable. In this way, the JM distance indicates which geomorphic units have statistically separable collections of roughness textures. Varying the size of W changes the degree of separability (Table V). On the MSH Pumice Plain, texture statistics calculated where $W = 11$ result in the largest JM distances ($JM = 2$ in each test: Table V). Eleven is therefore determined to be the most effective W size for this analysis and is used below in the analysis of variance (ANOVA).

The separability of geomorphic units based on individual texture statistics is tested using ANOVA following [47]. This method is different from the JM distance in that each texture statistic is interrogated individually, and all geomorphic units are compared simultaneously. ANOVA is a technique that evaluates separability while considering the reduced degrees of freedom present when more than two data sets are tested simultaneously, e.g., [47], [48]. It is employed here to assess the separability of all geomorphic units concurrently. Essentially, ANOVA determines the mean of test samples (values from each geomorphic unit within one texture layer) and then calculates confidence limits about each mean. Within in a specific layer, if geomorphic unit A has a mean value that is different from unit B's mean by an amount greater than their combined confidence intervals, A and B are separable. The relative tightness of the confidence interval depends on the particular hypothesis test used within ANOVA. Appropriate tests include: Fisher's least significant difference (LSD) test, the Scheffé tests, and the Bonferroni–Dunn test, e.g., [47]. Of the three tests, Fisher's LSD requires the smallest differences between unit means to conclude that the units are separable, as it produces the tightest confidence intervals about the unit means. However, in doing so, the possibility of falsely concluding two geomorphic units are separable is highest. Conversely, the Scheffé test requires the largest differences between unit means, and therefore the possibility of falsely concluding two geomorphic units are indistinguishable is highest. The Bonferroni–Dunn test produces intervals somewhere between the other two in size and is therefore the chosen test employed here.

The ANOVA results are given in Table VI. Units that have unique (from all other units) textures are marked with a check () in the matrix. There is a check in each texture column indicating that, when $W = 11$, each roughness texture statistic can be used to segregate one or more geomorphic units. In addition, there is a check in all but one row, indicating that each geomorphic unit (except DCh) can be differentiated based on one or more statistic (Fig. 7). Six or more units (including UNc) have unique μ, *HOM*, *ENT*, or *SMT* distributions. Conversely, *VAR*, *CON*, *DIS*, and *COR* can only be used to differentiate three or fewer geomorphic units. MBr, SbR, SbF, and DAd have statistically separable distributions from all other units in four or more texture statistics.

V. DISCUSSION

A. Preferred Set of Textural and Topographic Measures

The measures capable of differentiating the most geomorphic units on the Pumice Plain are: μ, *HOM, ENT*, and *SMT* (Table VI). Only three are necessary for visualization. *HOM* and *SMT* are closely correlated (Fig. 7) and describe similar patterns. *SMT* and *ENT* are both uniformity statistics, whereas HOM is a smoothness statistic [39], [41]. Therefore, μ, *HOM* and *ENT* are selected as the most instructive and preferred set of topographic and textural measures to describe the Pumice Plain features. These three measures are employed in a red/green/blue visualization (Fig. 5). Variations in μ, *HOM*, and *ENT* are inspected and found to aid in interpreting the geomorphic evolution of the region.

B. Geomorphology and Texture Interpretations

North-south trending gullies, partially filled with blocks, and bound by parallel ridges, dominate the north-facing slope in the southernmost portion of the study area (SbF: Fig. 5). This combination produces high μ and *HOM* (Fig. 7) from consistently high roughness values. The gullies were carved into pre-1980 lava flows and used by lahars to drain onto the Pumice Plain [23]. At the base of the steep slope, BrR and LPl produce a broad debris fan with High *ENT* generated by the random mantle of lithic boulders. These two units were differentiated in the field by the presence (LPl) or absence (BrR) of pumice lobes, and texturally by LPl having significantly higher μ than BrR. Both units were deposited by lahars and broadly correlate with Unit 1 (BrR) and Unit 2 (LPl) from [23], produced in the March 19, 1982 transient-lake breakout event. The sudden slope change and fan widening at the base of the scarp caused the lahars to drop their sediment (lithic boulders) and bury the pumice deposits completely (BrR) or, when boulder supply was limited, partially (LPl). Once enough lithics collected to sufficiently hinder flow passage through the Pumice Plain, deep, high-*ENT* channels (DCh) were carved to the west toward the Toutle River. DCh contains wide, active drainage channels with walls of unconsolidated pumice and ash and a floor of lithic boulders. The juxtaposition of these dissimilar roughness features produces high *ENT* and μ. Pumice lobes that were spared inundation by lahars (QPl) remain largely pristine and exhibit raised levees with coarse snouts and margins, as they did soon after deposition [17], [21]. QPl regions have higher μ than do BrR and LPl, as fluvial processes have not planed-off or buried the lobes and levees of QPl. However, QPl also has higher *HOM* and lower *ENT* than both LPl and BrR. This suggests that although pristine pumice-flow deposits are rougher than lahar-altered deposits, the distribution of lobes and levees is more uniform and ordered in undisturbed facies (QPl)

TABLE VI
SEPARABILITY MATRIX

		Roughness Texture								
		μ	σ^2	*HOM*	*CON*	*DIS*	*ENT*	*SMT*	*COR*	*Total Sep.*
Geomorphic Units	BrR	BSb	LPl,BSb,SbF	✓	BSb,SbF	BSb,LPl,DCh	DCh,LPl	LPl	QPl	1
	BSb	BrR	SbM,LPl,BrR	LPl,BrR	LPl,BrR	LPl,BrR,DCh	Dah	PPt	✓	1
	DCh	DAd	PPt	DAd	PPt	BSb,LPl,BrR	BrR,LPl	SbM	LTl	0
	LPl	✓	SbM,QPl,BSb,BrR	BSb	SbM,BSb	BSb,BrR,DCh	DCh,BrR	BrR	SbM	1
	MBr	✓	SbM	✓	SbM,QPl	✓	✓	✓	✓	6
	PPt	✓	DCh	✓	DCh	Unc,Dah	✓	BSb	SbF	3
	QPl	✓	SbM,LPl	SbM	SbM,MBr	SbM	✓	✓	SbM,BrR	3
	DAd	DCh,SbF	✓	DCh	✓	PPt	BSb	✓	✓	4
	SbF	DAd	BrR	✓	BrR	✓	✓	✓	PPt	4
	SbM	✓	QPl,LPl,BSb	QPl	MBr,QPl,LPl	QPl	✓	DCh	LPl,QPl	2
	SbR	✓	UNc	✓	✓	✓	✓	✓	DCh	6
	UNc[1]	✓	LTl	✓	✓	PPt	✓	✓	✓	6
Total Separable		7	1	6	3	3	7	6	4	

A "✓" indicates that the geomorphic unit has a unique texture distribution; unit labels in the cell indicate non-unique textures.
[1]UNc is unclassified. White columns (μ, HOM, and ENT) are displayed in the RGB composite (Fig. 5).

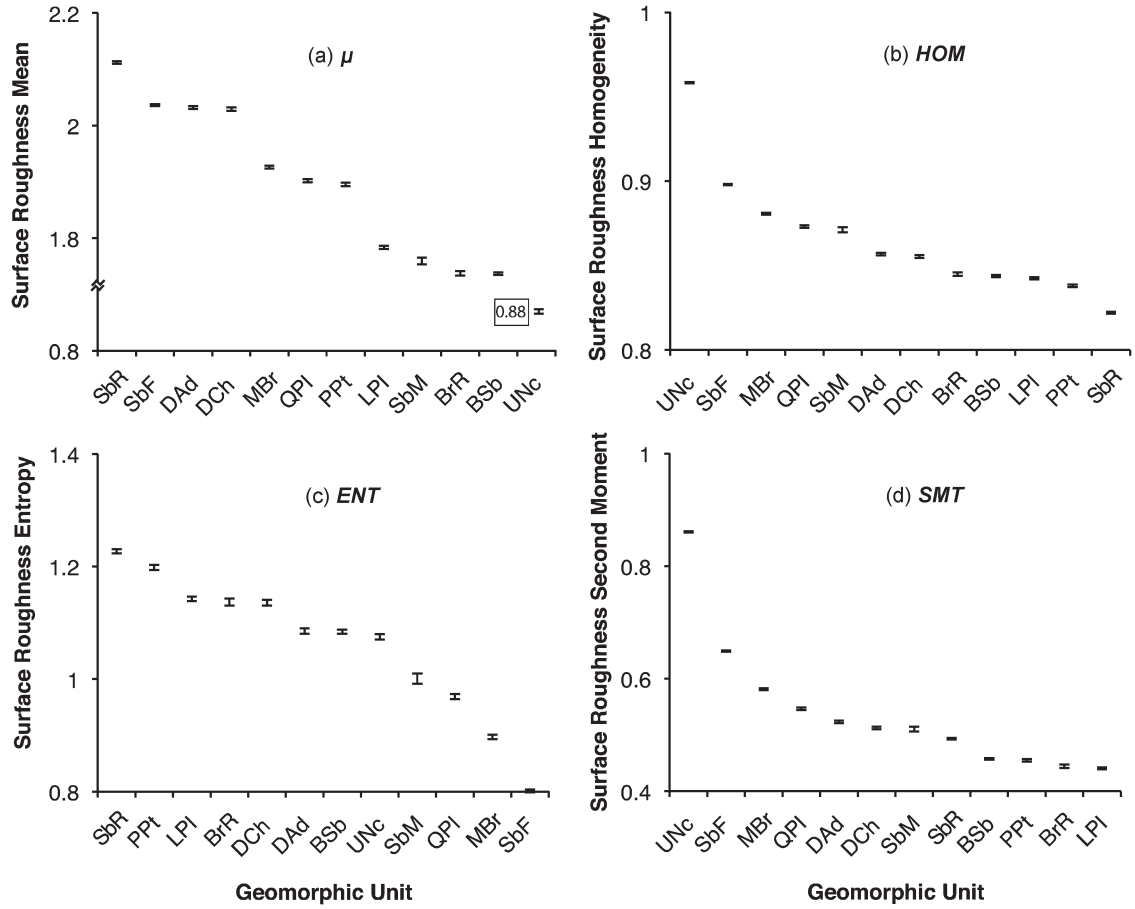

Fig. 7. Local roughness (a) μ, (b) Homogeneity (HOM), (c) Entropy (ENT), and (d) Second Moment (SMT) where $R_n = 5$ m and $W = 11$ pixels. Error bars represent the 95% confidence intervals calculated using ANOVA with the Bonferroni–Dunn test (following [47]). If the error bars of two or more geomorphic units overlap in the vertical dimension, the units are indistinguishable. If they do not, there is a 95% certainty that the geomorphic units are unique.

than the distribution of large blocks and ridges are after lahar perturbation (BrR and LPl).

BSb has low μ (Figs. 5 and 7), indicating that it consists of generally smooth regions. It has a uniquely high *COR* distribution, likely a result of fluvial organization of large blocks and sand bars in an active channel where sediment is reworked and in ample supply. Other reworked volcaniclastic units (MBr and PPt) have similarly moderate μ values, but have vastly different *ENT* and *HOM*. MBr has high *HOM* and low *ENT*, possibly due to the clast sorting and drainage organization within small alluvial fans common in MBr. PPt has high *ENT* and low *HOM*, indicating that stream terrace deposition and dissection (responsible for the deposition of this unit) produce far less organized deposits than do alluvial fan processes. SbM is significantly smoother (μ) than QPl, but the two are otherwise largely indistinguishable. This suggests that

TABLE VII
SUMMARY OF ROUGHNESS ELEMENTS CAPTURED BY THE ANALYSIS AND WITHIN EACH GEOMORPHIC UNIT

Label	Unit	Repeating feature	Length (m)	Width (m)	Height or depth (m)	Spacing (m)
BrR	Breccia ridges	Lithic ridges	10 - 100	2 - 3	0.5 - 1	5 - 8
BSb	Braided streams	Gravel & sand bars	10 - 20	2 - 4	0.5 - 1	2 - 4
DCh	Deep steep-walled channels	Canyon walls	10 - 400[a]	0 - 30	10 - 20	50 - 100
		Gravel & sand bars	10 - 20	2 - 4	0.5 - 1.5	2 - 4
LPl	Lithic armored pumice lobes	Pumice lobes	5 - 20	5 - 10	0.5 - 1.5	2 - 10
MBr	Mixed Breccias	Drainage channels	100 - 500	5 - 20	1 - 2	50 - 200
PPt	Pumice rich plateaus	Drainage channels	50 - 100	5 - 20	1 - 2	50 - 100
		Terraces	50 - 200	50 - 200	1 - 3	5 - 20
QPl	Quasi-pristine lobate fans	Pumice lobes	5 -20	5 - 10	0.5 - 1	1 - 3
DAd	Debris avalanche deposits	Hummocks	100 - 300	50 - 100	10 - 100	100 - 300
SbF	Substrate flanks	Ribs	10- 500	20 - 100	5 - 20	10 - 30
SbM	Substrate mounds	Clastic mounds	20 - 100	20 - 50	0.5 - 2	10 - 50
SbR	Substrate Ridges	Ridges	100 - 1500	100 - 1000	10 - 200	50 - 500

[a] Length of uninterrupted wall segment

SbM is a more subdued version of QPl and that it has been inundated by lahars but not eroded to the extent of DCh, and not buried by lithics to the extent of LPl and BrR.

SbR has the highest μ and *ENT*, and the lowest *HOM* of all the geomorphic units (Figs. 5 and 7). It is an intimate mixture of pyroclastic material and lava flows and has the roughest and most irregular surface of all the units. DAd contains a similar mixture of materials and is similarly rough, but has much lower *ENT* and higher *HOM*. Deposits of the DAd unit were transported in a debris avalanche whereas SbR remained *in situ* [14]. The juxtaposition of two contrasting materials (lava and pyroclasts) in an irregular fashion within both units, is likely responsible for the extremely high μ, but in DAd an avalanche organized the mixture somewhat at the scale of the analysis (tens of meters), lowering *ENT* and increasing *HOM*.

C. Utility of Roughness Texture

Lahar deposits, lava flows, pumice-rich, and fluvial units all have unique surface roughness textures. The sizes (Table VII) and patterns of roughness elements (blocks, boulders, channels, lobes, ridges, and gullies) for each surface type are unique and therefore produce unique patterns. Here, we present a generalized regime diagram (Fig. 8) potentially beneficial for using roughness texture to differentiate deposits elsewhere.

Eroded lava flow units have high μ because their surfaces are highly variable. (Note that pristine lava flow units were not observed here.) Pyroclastic flow deposits have moderate μ, low *ENT*, and high *HOM* in comparison. Pyroclastic deposits are generally smoother (where $R_n = 5$ m), and roughness patterns are more ordered and less extreme than are eroded lava flows. Lahar inundation affects pyroclastic deposits in two contrasting ways. First, eroding channels into pyroclastic deposits makes them rougher and less organized, increasing μ and *ENT* and lowering *HOM*. Second, deposition of material carried by lahars decreases μ and *HOM* and increases ENT by making the deposits smoother and less organized. Small alluvial fans are organized and smooth features, producing low μ and *ENT*, and high *HOM*. These relationships hold and are significant for analysis of the MSH Pumice Plain; with further verification by testing at other locations, it is hoped that Fig. 8 could eventually be applicable to generic interpretations in volcanic and fluvio-volcanic environments elsewhere.

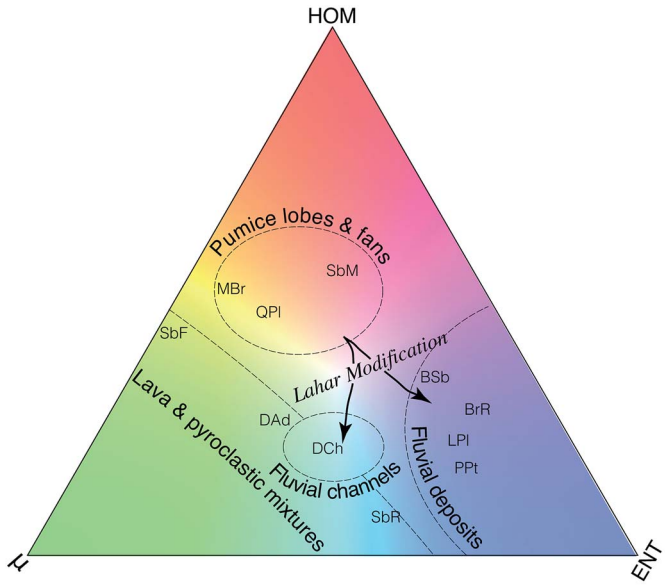

Fig. 8. Generalized texture ternary diagram, showing the relative textural differences observed in the Pumice Plain geomorphic units. Colors correspond to the relative importance of *HOM* (red) μ (green) and *ENT* (blue). Pumice lobes and fans occupy the center of the diagram, but after lahar modification their morphology is changed by one of either two ways: when erosion is dominant and channels are produced, *HOM* decreases whereas μ and *ENT* increase slightly. However, if deposition dominates, *HOM* and μ decrease and *ENT* increases sharply. This suggests that although lahar channels are rougher than lahar deposits produced with the same pyroclastic material, lahar deposits have a much more random distribution of blocks and ridges than both pristine pumice deposits or lahar channels.

The techniques described here are applicable to the analysis of any air or spaceborne LiDAR data sets. If, as recommended by the National Research Council in their 2007 Decadal Survey, the LiDAR Surface Topography (LIST) mission is flown [49], the resulting high-resolution global data set would provide a multitude of opportunities to use surface roughness texture mapping.

Any texture analysis should include a range of search neighborhood (W) sizes. Here, $W = 11$ is a preferred number of pixels for patterns to develop. Smaller window sizes were too restrictive, and local heterogeneities within the geomorphic units dominated the texture. Larger windows averaged too much information in each calculation and reduced the ability of roughness texture to differentiate geomorphic units. The broad

fans and slopes analyzed in this work produce patterns that are consistent over tens of meters and properly characterizing them using roughness texture requires a search neighborhood (W) of a similar scale. Subsequent studies to characterize the texture of smaller or larger features will likely require that W values be adjusted accordingly.

VI. Conclusion

A combination of field and remote sensing-based mapping techniques are used to differentiate and interpret eroded volcanic deposits and terrain around MSH, Washington.

1) Surface roughness texture mapping is well suited for locating and describing both pristine and eroded volcanic deposits. Geomorphic units mapped in the field have unique roughness texture that can be used to differentiate volcanic materials.
2) Defining appropriate roughness neighborhood and texture window sizes is critical to interpretation of the results. The resolution of the topographic data, as well as the desired application needs to be considered before texture maps are derived and utilized.
3) Pumice-flow deposits are moderately rough and have well-organized patterns of lobes and large blocks. Inundation of a pristine pumice deposit by mudflows decreases the organization and changes the general roughness of the surface. If the mudflow is losing energy and buries the pumice with an even layer of lithics, roughness decreases. If, conversely, the mudflow is fast moving and partially erodes the pumice, roughness increases.
4) Surface roughness texture mapping can be undertaken for remote environments rapidly and has clear applications for terrestrial as well as planetary volcanology. The method aids identification of volcanic and fluvio-volcanic terrains around volcanic edifices and can be applied where little is known about the terrain. It could be used in a range of applications including rapid hazard mapping to planetary mapping. Future applications could include the use of LIST data if NASA successfully flies this mission.

Acknowledgment

The authors thank P. Frenzen, B. Brand, and J. Bishop for logistical and field assistance at MSH; and G. Neumann and, J. Sauber-Rosenber for assistance with processing the LiDAR data at the NASA Goddard Space Flight Center. The authors also thank two anonymous reviewers for their comments.

References

[1] I. D. Novak and N. Soulakellis, "Identifying geomorphic features using LANDSAT-5/TM data processing techniques on Lesvos, Greece," *Geomorphology*, vol. 34, no. 1/2, pp. 101–109, Aug. 2000.

[2] G. Miliaresis, "The terrain signatures of administrative units: A tool for environmental assessment," *Environ. Monit. Assess.*, vol. 150, no. 1–4, pp. 385–396, Mar. 2009.

[3] D. Zouzias, G. C. Miliaresis, and K. S. Seymour, "Interpretation of Nisyros volcanic terrain using land surface parameters generated from the ASTER Global digital elevation model," *J. Volcanol. Geotherm. Res.*, vol. 200, no. 3/4, pp. 159–170, Mar. 2011.

[4] M. C. Gardeweg and R. S. J. Sparks, "Evolution of Lascar volcano, northern Chile," *J. Geol. Soc. Lond.*, vol. 155, no. 1, pp. 89–104, Feb. 1998.

[5] P. Lipman and D. Mullineaux, "The 1980 Eruptions of Mount St. Helens," USGS, Washington, DC, USA, Prof. Paper 1250, 1981.

[6] P. D. Rowley, M. A. Kuntz, and N. S. Macleod, "Pyroclastic flow deposits," in *The 1980 Eruptions of Mount St. Helens, Washington*, vol. 1250, P. Lipman and D. Mullineaux, Eds. Washington, DC, USA: USGS, 1981, pp. 489–512, Prof. Paper 1250.

[7] A. D. Howard, M. E. Keetch, and C. L. Vincent, "Topological and geometrical properties of braided streams," *Water Resources Res.*, vol. 6, no. 6, pp. 1674–1688, Jan. 1970.

[8] P. Francis, *Volcanoes. A Planetary Perspective*. Oxford, U.K.: Oxford Univ. Press, 1993, p. 443.

[9] R. Wright, H. Garbeil, S. Baloga, and P. Mouginismark, "An assessment of shuttle radar topography mission digital elevation data for studies of volcano morphology," *Remote Sens. Environ.*, vol. 105, no. 1, pp. 41–53, Nov. 2006.

[10] S. L. de Silva, J. E. Bailey, K. E. Mandt, and J. M. Viramonte, "Yardangs in terrestrial ignimbrites: Synergistic remote and field observations on Earth with applications to Mars," *Planetary Space Sci.*, vol. 58, no. 4, pp. 459–471, Mar. 2010.

[11] P. Grosse, B. van Wyk de Vries, P. A. Euillades, M. Kervyn, and I. A. Petrinovic, "Systematic morphometric characterization of volcanic edifices using digital elevation models," *Geomorphology*, vol. 136, no. 1, pp. 114–131, Jan. 2012.

[12] R. L. Christiensen and D. W. Peterson, "Chronology of the 1980 eruptive activity," in *The 1980 Eruptions of Mount St. Helens, Washington*, P. Lipman and D. Mullineaux, Eds. Washington, DC, USA: USGS, 1981, pp. 17–30, Prof. Paper 1250.

[13] B. Voight, "Time scale of the first moments of the May 18 eruption," in *The 1980 Eruptions of Mount St. Helens, Washington*, P. Lipman and D. Mullineaux, Eds. Washington, DC, USA: USGS, 1981, p. 69, Prof Paper 1250.

[14] P. Lipman, "Geologic Map of proximal deposits and features of 1980 eruptions of Mount St. Helens, Washington," in *The 1980 Eruptions of Mount St. Helens, Washington*, P. Lipman and D. Mullineaux, Eds. Washington, DC, USA: USGS, 1981, p. Plate 1, Prof. Paper 1250.

[15] R. Hoblitt, "Observations of the eruptions of July 22 and August 7, 1980, at Mount St. Helens, Washington," USGS, Washington, DC, USA, Prof. Paper 1335, 1986.

[16] M. A. Kuntz, P. D. Rowley, N. S. Macleod, R. L. Reynolds, L. A. Mcbroome, A. M. Kaplan, and D. J. Lidke, "Petrography and particle-size distribution of pyroclastic-flow, ash-cloud, and surge deposits," in *The 1980 Eruptions of Mount St. Helens, Washington*, P. Lipman and D. Mullineaux, Eds. Washington, DC, USA: USGS, 1981, p. 525, Prof. Paper 1250.

[17] L. Wilson and J. Head, "Morphology and rheology of pyroclastic flows and their deposits, and guidelines for future observations," in *The 1980 Eruptions of Mount St. Helens, Washington*, P. W. Lipman and D. R. Mullineaux, Eds. Washington, DC, USA: USGS, 1981, pp. 513–524.

[18] J. H. Fink, M. C. Malin, R. E. D'Alli, and R. Greeley, "Rheological proprties of Mudflows associated with the spring 1980 eruptions of Mount St. Helens, Washington," *Geophys. Res. Lett.*, vol. 8, no. 1, pp. 43–46, Jan. 1981.

[19] R. J. Janda, K. M. Scott, K. M. Nolan, and H. A. Martinson, "Lahar Movement, effects, and deposits," in *The 1980 Eruptions of Mount St. Helens, Washington*, P. Lipman and D. Mullineaux, Eds. Washington, DC, USA: USGS, 1981, pp. 461–478, Prof. Paper 1250.

[20] R. B. Waitt, Jr., T. C. Pierson, and N. S. MacLeod, "Eruption-triggered avalanche, flood, and lahar at Mount St. Helens—Effects of winter snowpack," *Science*, vol. 221, no. 4618, pp. 1394–1397, Sep. 1983.

[21] C. A. Neal, "Textural and Morphologic Studies of Small-Volume Ignimbrite of Mount St. Helens, 1980," M.S. thesis, Arizona State Univ., Tempe, AZ, USA, 1986.

[22] J. W. Vallance, C. A. Gardner, W. E. Scott, R. M. Iverson, and T. C. Pierson, "Mount St. Helens: A 30-year legacy of volcanism," *EOS, Trans. Amer. Geophys. Union*, vol. 91, no. 19, pp. 169–180, May 2010.

[23] T. C. Pierson, Ed., *Hydrologic Consequences of Hot-Rock/Snowpack Interactions at Mount St. Helens Volcano, Washington*. Washington, DC, USA: USGS, p. 117, Prof. 1999.

[24] W. E. Scott, D. R. Sherrod, and C. A. Gardner, "Overview of 2004 to 2005, and continuing, eruption of Mount St. Helens, Washington," in *A Volcano Rekindled: The Renewed Eruption of Mount St. Helens, 2004–2006, no. October 2004*, D. R. Sherrod, W. E. Scott, and P. H. Stauffer, Eds. Washington, DC, USA: USGS, 2008, pp. 3–22, Prof. Paper.

[25] P. Devara, "Real-time monitoring of atmospheric aerosols using a computer-controlled lidar," *Atmos. Environ.*, vol. 29, no. 16, pp. 2205–2215, Aug. 1995.
[26] W. Carter, R. Shrestha, G. Tuell, D. Bloomquist, and M. Sartori, "Airborne laser swath mapping shines new light on Earth's topography," *EOS Trans.*, vol. 82, no. 46, pp. 549–555, Nov. 2001.
[27] F. Mazzarini, M. Pareschi, M. Favalli, I. Isola, S. Tarquini, and E. Boschi, "Lava flow identification and aging by means of lidar intensity: Mount Etna case," *J. Geophys. Res.*, vol. 112, no. B2, pp. B02 201-1–B02 201-19, Feb. 2007.
[28] M. Favalli, A. Fornaciai, F. Mazzarini, A. Harris, M. Neri, B. Behncke, M. Pareschi, S. Tarquini, and E. Boschi, "Evolution of an active lava flow field using a multitemporal LIDAR acquisition," *J. Geophys. Res.*, vol. 115, no. B11, p. B11 203, Nov. 2010.
[29] B. Csatho, T. Schenk, P. Kyle, T. Wilson, and W. Krabill, "Airborne laser swath mapping of the summit of Erebus volcano, Antarctica: Applications to geological mapping of a volcano," *J. Volcanol. Geotherm. Res.*, vol. 177, no. 3, pp. 531–548, Nov. 2008.
[30] A. R. Morris, F. S. Anderson, P. J. Mouginis-Mark, A. F. C. Haldemann, B. A. Brooks, and J. Foster, "Roughness of Hawaiian volcanic terrains," *J. Geophys. Res.*, vol. 113, no. E12, pp. E12 007-1–E12 007-20, Dec. 2008.
[31] J. D. Pelletier, H. Mitasova, R. S. Harmon, and M. Overton, "The effects of interdune vegetation changes on eolian dune field evolution: A numerical-modeling case study at Jockey's Ridge, North Carolina, USA," *Earth Surf. Process. Landforms*, vol. 34, no. 9, pp. 1245–1254, Jul. 2009.
[32] J. Mundt, D. Streutker, and N. F. Glenn, "Mapping sagebrush distribution using fusion of hyperspectral and lidar classifications," *Photogramm. Eng. Remote Sens.*, vol. 72, no. 1, pp. 47–54, Jan. 2006.
[33] I. J. Davenport, N. Holden, and R. J. Gurney, "Characterizing errors in airborne laser altimetry data to extract soil roughness," *IEEE Trans. Geosci. Remote Sens.*, vol. 2, no. 10, pp. 2130–2141, Oct. 2004.
[34] J. B. Sankey, N. F. Glenn, M. J. Germino, A. I. N. Gironella, and G. D. Thackray, "Relationships of aeolian erosion and deposition with LiDAR-derived landscape surface roughness following wildfire," *Geomorphology*, vol. 119, no. 1/2, pp. 135–145, Jun. 2010.
[35] N. Glenn, D. Streutker, and D. Chadwick, "Analysis of LiDAR-derived topographic information for characterizing and differentiating landslide morphology and activity," *Geomorphology*, vol. 73, no. 1/2, pp. 131–148, Jan. 2006.
[36] L. S. Glaze and S. M. Baloga, "Topographic variability on Mars: Implications for lava flow modeling," *J. Geophys. Res.*, vol. 112, no. E8, p. E08 006, Aug. 2007.
[37] M. A. Rosenburg, O. Aharonson, J. W. Head, M. A. Kreslavsky, E. Mazarico, G. A. Neumann, D. E. Smith, M. H. Torrence, and M. T. Zuber, "Global surface slopes and roughness of the moon from the lunar orbiter laser altimeter," *J. Geophys. Res.*, vol. 116, no. E2, p. E02 001, Feb. 2011.
[38] R. M. Haralick, K. Shanmugam, and I. Dinstein, "Textural features for image classification," *IEEE Trans. Syst., Man, Cybern.*, vol. SMC-3, no. 6, pp. 610–621, Nov. 1973.
[39] O. C. R. Filho, P. M. Treitz, E. D. Soulis, P. J. Howarth, and N. Kouwen, "Texture processing of synthetic aperture radar data using second-order spaitail statistics," *Comput. Geosci.*, vol. 22, no. 1, pp. 27–34, Feb. 1996.
[40] D. A. Clausi, "An analysis of co-occurrence texture statistics as a function of grey level quantization," *Can. J. Remote Sens.*, vol. 28, no. 1, pp. 45–62, Feb. 2002.
[41] Y. Zhang, "Optimization of building detection in satellite images by combining multispectral classification and texture filtering," *ISPRS J. Photogramm. Remote Sens.*, vol. 54, no. 1, pp. 50–60, Feb. 1999.
[42] D. J. Harding, *TerraPoint LIDAR Mapping Instrumentation and Methodology*. Woodlands, TX, USA: TerraPoint, LLC, 2004, pp. 1–22.
[43] J. Bishop, "Early primary succession on Mount St. Helens: Impact of insect herbivores on colonizing lupines," *Ecology*, vol. 83, no. 1, pp. 191–202, Jan. 2002.
[44] C. A. Hopson, "Geologic Map of Mount St. Helens, Washington Prior to the 1980 Eruption," USGS, Washington, DC, USA, USGS Open-File Rep. 02-468, 2008.
[45] P. H. Swain and S. Davis, *Remote Sensing: The Quantitative Approach*. New York, USA: McGraw-Hill, 1978.
[46] J. A. Richards, *Remote Sensing Digital Image Analysis*. Berlin, Germany: Springer-Verlag, 1999, p. 240.
[47] D. J. Sheskin, *Handbook of Parametric and Nonparametric Statistical Procedures*. Boca Raton, FL, USA: CRC Press, 1997, p. 719.
[48] G. W. Snedecor and W. G. Cochran, *Statistical Methods*., 6th ed. Iowa City, IA, USA: Univ. of Iowa Press, 1967, p. 593.
[49] A. W. Yu, M. A. Krainak, D. J. Harding, J. B. Abshire, and X. Sun, "A spaceborne lidar for high-resolution topographic mapping of the earth's surface," in *Proc. SPIE Newsroom*, 2010, pp. 1–3.

Patrick L. Whelley received the B.S. and M.S. degrees in geological sciences from Arizona State University in Tempe, AZ, in 2005 and 2007, respectively, and the Ph.D. degree in geology from the University at Buffalo, SUNY in Buffalo, NY, in 2012.

Currently, he is a Research Fellow at the Earth Observatory of Singapore within Nanyang Technological University in Singapore. His research interests include combining remote sensing and field geology observations of volcanic deposit morphology to study physical volcanology and geohazards, as well as studying aeolian and volcanic processes on the terrestrial planets. He has authored or coauthored 19 peer-reviewed publications.

Lori S. Glaze received the B.A. and M.S. degrees in physics from the University of Texas, Arlington, TX, in 1985 and 1989, respectively, and the Ph.D. degree in environmental science from Lancaster University, Lancaster, U.K., in 1994.

She has worked at the California Institute of Technology Jet Propulsion Laboratory, Proxemy Research Inc., and NASA Goddard Space Flight Center (GSFC). Currently, she is an Associate Chief of the Planetary Geodynamics Laboratory at NASA GSFC. Her research interests are focused on physical modeling of volcanic processes, including lava flow emplacement and explosive eruption column dynamics, on Earth, Venus, Mars, and Io. She served on the Inner Planets Panel of the 2009–2010 National Research Council Planetary Decadal Survey and is the Chair of the NASA Venus Exploration Analysis Group. She has 47 peer-reviewed publications and is a coauthor of a book on volcanic plumes.

Eliza S. Calder received the Ph.D. degree from The University of Bristol, Bristol, U.K., in 1999.

She is an Associate Professor at the University at Buffalo, Buffalo, NY. She has broad interests across physical volcanology. In particular, her research focuses on the processes associated with explosive volcanism including the generation and emplacement of volcanic plumes and pyroclastic density currents, through the application of multidisciplinary approaches and techniques. She also enjoys the applied aspects of work in this discipline, including the study of volcanic activity through volcano monitoring and studies related to hazard assessment and mitigation. She works in direct connection with several volcano observatories in the Caribbean and Latin America. She has authored or coauthored 35 peer-reviewed publications and contributed to two books.

David J. Harding received the B.S. and Ph.D. degrees in geological sciences from Cornell University, Ithaca, NY, in 1980 and 1988, respectively.

Since 1991, he has been a Research Scientist with the NASA Goddard Space Flight Center, Greenbelt, MD, USA, where he currently works in the Planetary Geodynamics Laboratory, Sciences, and Exploration Directorate. He conducts research in the topographic expression of land surface processes and the physical properties of vegetation, snow, ice, and water, in particular by developing and utilizing advanced airborne and space-based laser altimeter systems. He is a Principal Investigator for the airborne Slope Imaging Multi-polarization Photon-Counting Lidar, developed through the NASA Instrument Incubator Program. He was a Member of the Ice, Cloud, and Land Elevation Satellite (ICESat) Science Team and is now a Member of the ICESat-2 Science Definition Team. In addition, he represented NASA in the Puget Sound Lidar Consortium that conducted comprehensive lidar mapping in the Puget Sound region and Cascades Range, WA. He has authored or coauthored 45 conference proceedings and peer-reviewed papers.